

# Implicit and explicit finite element models predict the mechanical response of calcium phosphate-titanium cranial implants

**Journal Article****Author(s):**

Lewin, Susanne; Fleps, Ingmar; Neuhaus, Dominique; Öhman-Mägi, Caroline; Ferguson, Stephen J.; Persson, Cecilia; Helgason, Benedikt

**Publication date:**

2020-12

**Permanent link:**

<https://doi.org/10.3929/ethz-b-000447662>

**Rights / license:**

[Creative Commons Attribution 4.0 International](#)

**Originally published in:**

Journal of the Mechanical Behavior of Biomedical Materials 112, <https://doi.org/10.1016/j.jmbbm.2020.104085>



# Implicit and explicit finite element models predict the mechanical response of calcium phosphate-titanium cranial implants

Susanne Lewin<sup>a,\*</sup>, Ingmar Fleps<sup>b</sup>, Dominique Neuhaus<sup>b</sup>, Caroline Öhman-Mägi<sup>a</sup>, Stephen J. Ferguson<sup>b</sup>, Cecilia Persson<sup>a</sup>, Benedikt Helgason<sup>b</sup>

<sup>a</sup> Department of Materials Science and Engineering, Uppsala University, Uppsala, Sweden

<sup>b</sup> Institute for Biomechanics, ETH Zurich, Zurich, Switzerland

## ARTICLE INFO

### Keywords:

Mechanical properties  
Cranial implant  
Bioceramics  
Computational models  
Impact

## ABSTRACT

The structural integrity of cranial implants is of great clinical importance, as they aim to provide cerebral protection after neurosurgery or trauma. With the increased use of patient-specific implants, the mechanical response of each implant cannot be characterized experimentally in a practical way. However, computational models provide an excellent possibility for efficiently predicting the mechanical response of patient-specific implants. This study developed finite element models (FEMs) of titanium-reinforced calcium phosphate (CaP-Ti) implants. The models were validated with previously obtained experimental data for two different CaP-Ti implant designs (D1 and D2), in which generically shaped implant specimens were loaded in compression at either quasi-static (1 mm/min) or impact (5 kg, 1.52 m/s) loading rates.

The FEMs showed agreement with experimental data in the force-displacement response for both implant designs. The implicit FEMs predicted the peak load with an underestimation for D1 (9%) and an overestimation for D2 (11%). Furthermore, the shape of the force-displacement curves were well predicted. In the explicit FEMs, the first part of the force-displacement response showed 5% difference for D1 and 2% difference for D2, with respect to the experimentally derived peak loads. The explicit FEMs efficiently predicted the maximum displacements with 1% and 4% difference for D1 and D2, respectively. Compared to the CaP-Ti implant, an average parietal cranial bone FEM showed a stiffer response, greater energy absorption and less deformation under the same impact conditions.

The framework developed for modelling the CaP-Ti implants has a potential for modelling CaP materials in other composite implants in future studies since it only used literature based input and matched boundary conditions. Furthermore, the developed FEMs make an important contribution to future evaluations of patient-specific CaP-Ti cranial implant designs in various loading scenarios.

## 1. Introduction

Cranial defects caused by trauma or neurosurgery are commonly reconstructed using autologous bone or synthetic implants. The procedure has a high clinical complication rate (~20%), where infection is the most common complication for synthetic cranial implants (van de Vijfeijken et al., 2018). These implants have commonly been made of bioinert materials, e.g. PMMA. The outcome could potentially be improved by using osteoconductive and bioactive materials (Engstrand, 2012). One such recently introduced cranial implant, a patient-specific calcium phosphate-titanium (CaP-Ti) implant (OssDesign Cranial, OssDesign, Uppsala, Sweden), has shown promising clinical outcomes in

terms of low complication rates (Engstrand et al., 2014; Kihlström Burenstam Linder et al., 2019; Sundblom et al., 2018). In a recent retrospective study of 50 patients, only 7.5% developed complications which lead to implant removal. Since this patient cohort previously had a 64% failure rate with autologous bone or other synthetic implants (Kihlström Burenstam Linder et al., 2019), this outcome was considered particularly promising. An important function of cranial implants is to provide cerebral protection. The positive clinical results could increase the clinical use of the CaP-Ti implant, which motivates scientific investigations of their protective capability and structural integrity. Moreover, while medical imaging and additive manufacturing have enabled the production of patient-specific implants in a relatively

\* Corresponding author. Div. of Applied Materials Science, Department of Materials Science and Engineering Uppsala University, Box 35, 751 03, Uppsala, Sweden.  
E-mail address: [susanne.lewin@angstrom.uu.se](mailto:susanne.lewin@angstrom.uu.se) (S. Lewin).

<https://doi.org/10.1016/j.jmbbm.2020.104085>

Received 2 April 2020; Received in revised form 14 August 2020; Accepted 8 September 2020

Available online 20 September 2020

1751-6161/© 2020 The Authors. Published by Elsevier Ltd. This is an open access article under the CC BY license (<http://creativecommons.org/licenses/by/4.0/>).

straight-forward manner (Zegers et al., 2017; Lethaus et al., 2014), experimental evaluation of each patient-specific design is not possible. The use of computational models for assessing the mechanical behavior of cranial implants could be a solution to these challenges.

In experimental studies, cranial implants have mainly been evaluated under quasi-static compressive loading using an indenter (Berretta et al., 2018; El Halabi et al., 2011; Lethaus et al., 2011; Piitulainen et al., 2017; Matic and Manson, 2004; Ono et al., 1998). However, impact loading is most likely a more realistic loading to which a skull is subjected. This type of loading has previously only been investigated for cranial implants in a few experimental studies (Matic and Manson, 2004; Ambrogio et al., 2018; Lewin et al., 2020). Computational simulations have made interesting contributions in structural evaluations of a few types of cranial implants. Studies have evaluated differences in design and location of implant fixation (El Halabi et al., 2011; Ridwan-Pramana et al., 2016; Ridwan-Pramana et al., 2017; Marcián et al., 2019). Others have varied the implant thickness of several materials, with the purpose to assess bone-implant load transfer (Marcián et al., 2019; Persson et al., 2018). The majority of these studies assume quasi-static loading rate, linear elastic materials, and linear geometry (El Halabi et al., 2011; Ridwan-Pramana et al., 2017; Persson et al., 2018). So far, only one computational study has investigated cranial implants under impact loading: Garcia-Gonzalez et al. (2017) placed solid PEEK and porous HA implants in a FE head model, and demonstrated differences in the mechanical response at different impact velocities (Garcia-Gonzalez et al., 2017). It would be of considerable interest to simulate impact loading also for other types of cranial implants. Furthermore, it is important to model the mechanical response of these implants up to failure loads in order to assess the implant response during trauma – which has so far not been studied.

Our study focuses on validation of computational models of the patient-specific calcium phosphate-titanium (CaP-Ti) implant, which has a somewhat more complex structure than other commonly used implants. CaP tiles in the implant aim to improve biocompatibility and osseointegration, but are inherently brittle. For increased structural support, a titanium structure forms the basis of the implant. In a recent experimental study, we measured the mechanical response of generic CaP-Ti implant specimens, both under quasi-static and impact loading (Lewin et al., 2020). Two implant designs were evaluated. The first design was conceptually representative of the clinically used implants (Design 1 – D1), and the second was modified in order to facilitate additive manufacturing of the titanium structure (Design 2 – D2). The data obtained in that study offers experimental reference data for validation of finite element models (FEMs) of the CaP-Ti implant. Furthermore, modelling CaP materials in a complicated composite system is so far unexplored.

The primary aim of the present study was to develop a finite element modelling approach for CaP-Ti implant designs, and to validate it against experimental data of two implant designs at impact and quasi-static loading rates. A secondary aim was to estimate the mechanical response for cranial bone under the same impact loading, and to compare this outcome to the mechanical response of the implants.

## 2. Materials and methods

### 2.1. Experimental testing

The mechanical testing of the CaP-Ti implants has been reported previously (Lewin et al., 2020), an overview is provided below for clarity and context. Implant specimens of two different designs, with a generic shape ( $\phi = 80$  mm) were used (Fig. 1). The radius of the specimen curvature was 90 mm. The first, Design 1 (D1), was conceptually representative of the current clinically used implants (OssDsign Cranial, OssDsign, Uppsala, Sweden). In the modified, Design 2 (D2), simplifications were made in the titanium structure with the purpose of facilitating the additive manufacturing process while aiming to maintain implant strength. In D1, the rods in the titanium structure had a rectangular cross-section ( $0.6 \times 1.6$  mm<sup>2</sup>). The CaP tiles were hexagonal in shape with a thickness of 6 mm. The distance between the tiles was 1 mm at the top and 2 mm at the bottom of the implant. Deformation zones, i.e. 0.3 mm wide and 0.3 mm high notches intended to concentrate and control deformation, were placed between the CaP tiles in D1 (Fig. 1a). In D2, the cross-section of the rods in the titanium structure was circular ( $\phi = 1.2$  mm), and the deformation zones were excluded. The CaP tiles were generally larger and the shape was changed as the middle CaP tile in D2 was circular, and the other tiles were placed in a pattern surrounding the central tile (Fig. 1b). The titanium structures were additively manufactured in a titanium alloy (Ti-6Al-4V) using a powder bed fusion laser beam (L-PBF) process. The tiles were molded using a self-setting monetite-based CaP formulation (Engstrand et al., 2014). The implant specimens were provided by the implant manufacturer (OssDsign AB, Uppsala, Sweden).

In the experimental setup, a rigid hollow steel cylinder, was used to support the implants around the circumference during testing. The conical contact surfaces of the steel cylinder had the same incline as the implant edges. This conical hollow steel cylinder is hereinafter referred to as the conical steel support. In order to obtain firm contact between the ceramic tiles and the conical steel support, calcium phosphate cement was applied to the contact surface prior to placing the specimen on the support structure. In the quasi-static tests, the setup was mounted in a universal testing machine (AGS-X, Shimadzu Corp., Japan), and compressive load was applied using a hemispherical indenter ( $\phi = 40$

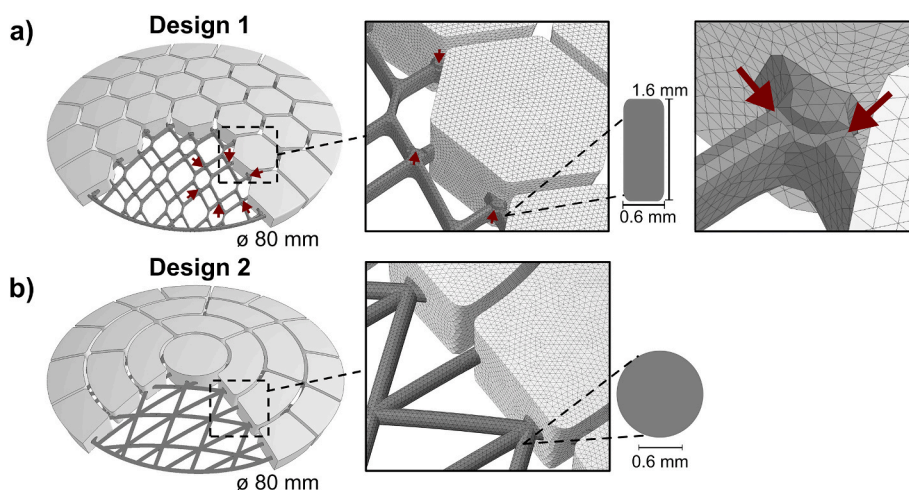


**Fig. 1.** Visualization of the two implant designs: D1 (a) and D2 (b). The models to the left show the full implants. Some of the CaP tiles have been removed in order to visualize the titanium structure. Around one of the removed tiles in D1, the locations of the deformation zones are marked with red arrows. The center images show a magnified part (including the mesh) of the titanium and the CaP tiles, and a magnification of the cross section of the titanium structure. The image to the far right shows a magnified part of D1 to visualize the mesh in one of the deformation zones (marked by red arrows). (For interpretation of the references to color in this figure legend, the reader is referred to the Web version of this article.)

mm). A silicone rubber sheet (thickness of 5 mm) was placed on top of the implants as a soft tissue surrogate. Next, the implants were loaded to failure at a displacement rate of 1 mm/min. In the impact test, the full setup, including the support, implant specimen and rubber sheet, was placed in a drop-tower rig (Fig. 2). The implants were loaded through a hemispherical indenter ( $\phi = 40$  mm) mounted on a carriage, with a total mass of 5 kg, which impacted with a speed of 1.52 m/s. A high-speed camera (IDT Y8-S2, Integrated Design Tools Inc., USA) recorded the displacement between carriage and support markers at 6800 frames/second (FPS) (Fig. 2). The force was measured at 13 600 Hz using a piezoelectric force sensor (208C04, PCB Piezotronics, Inc., USA) placed between the indenter and the carriage.

## 2.2. Finite element models

### 2.2.1. Model geometries

CAD-files of the titanium structure and the ceramic tiles, for both designs, were obtained from the implant manufacturer (OssDsign, Uppsala, Sweden) (Fig. 1). The hemispherical indenter ( $\phi = 40$  mm), and the surface of the conical steel support below the specimen were modelled to match the experimental setup. All parts were semi-automatically discretized with tetrahedral elements in a commercial pre-processor (Ansa 17.1.0, Beta CAE Systems, Switzerland). Parts of the resulting FE meshes are visualized in Fig. 1 for the CaP tiles and titanium structure of both implant designs.

### 2.2.2. Implicit models

The indenter and the conical steel support surface were modelled as a linear elastic material, with properties corresponding to steel (Young's modulus:  $E = 210$  GPa, and Poisson's ratio:  $\nu = 0.3$ ). All nodes on the outer edge of the support surface were fixed. The indenter was constrained from translation in x and y-direction (the coordinate system is visualized in Fig. 2). Loading was applied by a uniform displacement of the indenter, applied to all nodes on the upper surface of the indenter in z-direction. Contact pairs were defined with friction ( $\mu = 0.3$ ), between the CaP tiles and the conical steel support surface, and between the indenter and the CaP tiles. The nodes of the CaP tiles were tied to the titanium, assuming a perfect interface bonding between the tiles and the titanium structures. This assumption was chosen because the interface prior to the experiments was intact and the strong geometrical interlocking of the structures is likely to be dominant in the interaction between the CaP and the titanium structures.

The implicit models (including the implant, the indenter and the conical steel support surface) consisted of 3 122 970 and 2 612 654 elements for D1 and D2 respectively. The number of elements, element formulations, and the mean element edge length for the parts in the implants are presented in Table 1. The indenter and support surface were modelled with first order tetrahedral elements (LS-DYNA, element formulation 10). Tetrahedral elements of the first order were also used

for the titanium structure and the ceramic tiles in the implant, but another element formulation that takes nodal pressure into account in order to reduce volumetric locking (LS-DYNA, element formulation 13) was used (Bonet and Burton, 1998). The FEMs were solved with double precision in a commercial implicit solver (LS-DYNA R11.0.0, Livermore, CA, USA).

### 2.2.3. Explicit models

The models used for the implicit FEM simulations were used to set up the explicit FEMs. Additionally, the rubber sheet (5 mm thickness) was modelled in the explicit FEM. For the rubber sheet, a hyper-elastic Mooney-Rivlin material model (LS-DYNA, MAT 27) was used. The material model constants were reverse engineered from experimental results obtained for the silicone material in compression tests performed according to ISO 7743. The resulting Mooney-Rivlin constants were  $C_1 = 15 \times 10^{-5}$  and  $C_2 = 4 \times 10^{-5}$ .

The elements on the conical steel support surface were fixed in all directions. In addition to the contact pairs used in the implicit models, contact pairs were defined with friction ( $\mu = 0.3$ ) between the indenter and the rubber sheet, and between the rubber sheet and the CaP tiles. To stabilize the rubber sheet, an interior contact was defined. Gravity was applied to all parts of the model. The carriage mass (5 kg), and velocity measured from the drop-tower experiments (1.52 m/s) were applied to the indenter as initial conditions (Lewin et al., 2020).

Tetrahedral shell elements (LS-DYNA, element formulation 16) were used to mesh the indenter and the conical steel support surface. For the titanium, second order tetrahedral elements were used (LS-DYNA, element formulation 16). The CaP tiles were again represented by first order tetrahedral elements (LS-DYNA, element formulation 13). The number of elements (Table 1), for the explicit models were 3 103 202 and 2592 9970 for models D1 and D2, respectively. Comparison between the experimental setup and the FEMs can be seen in Fig. 2. The FEMs were solved with double precision in a commercial explicit solver (LS-DYNA R11.0.0, Livermore, CA, USA).

### 2.2.4. Material models: CaP and Ti-6Al-4V

The density and porosity (40%) of the monetite-based CaP material was provided by the implant manufacturer (OssDsign, Uppsala, Sweden). The CaP material properties (Table 2) were based on previous compression testing performed on the same CaP formulation, in which the deformation was measured by digital image correlation (Ajaxon et al., 2017). The strength for CaP materials is known to be lower in tension (Pittet and Lemaître, 2000; Ajaxon and Persson, 2017), however, data on tensile properties for CaP materials is limited due to experimental difficulties, caused by the brittle behavior. Moreover, diametral tensile tests, which are performed more frequently, do not correctly estimate the tensile strength for these types of materials (Pittet and Lemaître, 2000). Consequently, the tensile properties were based on experimental work (Charrière et al., 2001). They performed tensile and

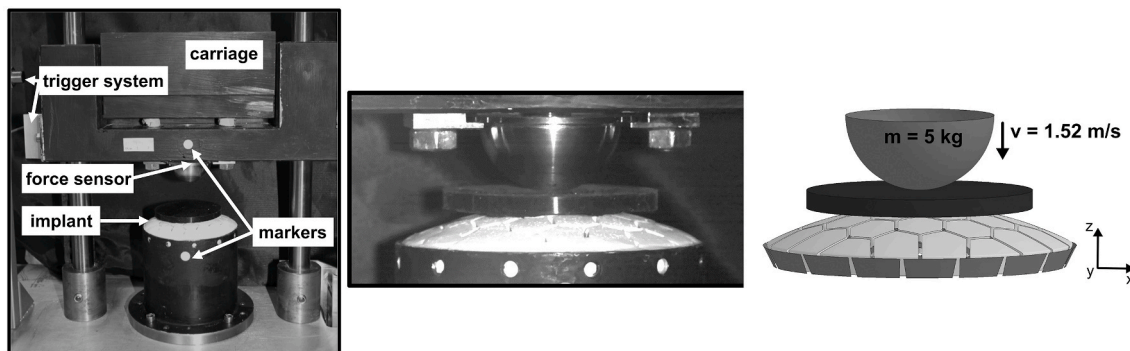


Fig. 2. Drop-tower experimental setup and computational model: The experimental setup – with the different parts marked in the image (left); a magnified image of the implant specimen and the indenter (middle); and the explicit FE-model (right).

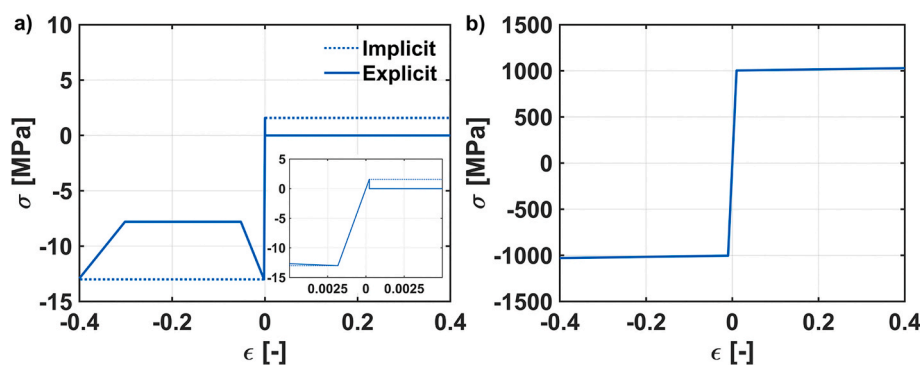
**Table 1**

Element type and number of elements for the implant parts in the implicit and explicit models.

Part	Number of elements		Element type	Element formulation		Mean element edge length [mm]	
	D1	D2		Implicit	Explicit	D1	D2
Titanium structure	402 913	387 259	tetrahedron	1st order (LS-DYNA, el. form 13)	2nd order (LS-DYNA, el. form 16)	0.33	0.36
CaP tiles	2 681 385	2186 834	tetrahedron	1st order (LS-DYNA, el. form 13)	1st order (LS-DYNA, el. form 13)	0.44	0.47

**Table 2**Material properties for the titanium alloy and CaP material (average  $\pm$  SD).

	$E$ [GPa]	$\nu$ [-]	$\sigma_y$ [MPa]	$\sigma_{UTS}$ [MPa]		Strain at break [%]
				tension	compression	
CaP	$7.1 \pm 1.0$ (Ajaxon et al., 2017)	$0.2 \pm 0.03$ (Ajaxon et al., 2017)	–	$1.6 \pm 0.19$ (Charrière et al., 2001)	$13 \pm 1.6$ (Ajaxon et al., 2017)	–
Ti6Al4V	$102.2 \pm 7.5$	0.3	$1003.6 \pm 21.1$	$1086.1 \pm 10.1$	–	$10.7 \pm 1.3$

**Fig. 3.** The material models implemented in the simulations for the CaP material (a) and the titanium alloy (b). For the CaP material model, the initial elastic part of the curve is shown in the bottom right corner (a).

compression tests using both a uniaxial and biaxial extensometer. The brushite in their tests had a similar compression strength (10.7 MPa) as our monetite-based ceramic. For these reasons, the ratio that Charrière et al. (2001) obtained between tensile and compression strength, was used in our study to estimate the tensile strength of our CaP material to 1.6 MPa (Table 2). A material model with tension-compression asymmetry (LS-DYNA, MAT 124) was implemented for the CaP material (Fig. 3). As fractures in the CaP material were observed experimentally before yielding of the titanium, damage was modelled by introducing softening both in compression and in tension after the strain of failure was reached (0.2%). The tensile stress was decreased to 10% of the tensile strength (to model catastrophic failure). The compression stress was decreased to 60% of the compression strength (motivated by the 40% porosity of the CaP). Thereafter, for an additional 30% strain in compression, densification was assumed. In the implicit models no damage was considered. Instead, perfect plasticity was assumed both in tension and compression (Fig. 3a).

The material properties for the titanium alloy were measured on tensile test specimens, produced to correspond to the geometry of the titanium structure in the D2 implants. The gauge length was 10 mm and the diameter 1.2 mm. The measured tensile strength (Table 2) agreed with previous tests on standard sized specimens produced with the same additive manufacturing process (Fousová et al., 2018). An elasto-plastic material model was used for the titanium alloy (LS-DYNA, MAT 024), see Fig. 3b. Stresses were recalculated from the nominal stress and strain (reported in Table 2) to the Cauchy stress and logarithmic strain before implementation into the FEMs.

### 2.3. Comparison between FEMs and experimental results

The response of each FEM was compared to the corresponding experimental data. The response was plotted from a force of 100 N, where the displacement was set to zero. This was done to minimize the influence of the toe-region created by the rubber sheet.

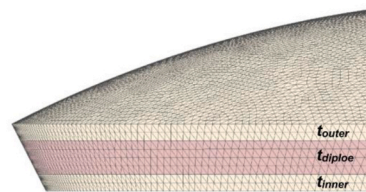
For the experimental quasi-static results, three curves were created; a curve for the average results, and a curve one standard deviation (SD) above and below the average curve. The compliance of the rubber sheet was subtracted from the quasi-static experimental results in the comparison to the implicit FEM. In the subtraction, a spline interpolation of silicone rubber test data was used (5 mm silicon sheet tested in compression at 1 mm/min with the same indenter as the one used in the implant testing). The force measured in the quasi-static tests was compared to the section force for the indenter in the implicit FEM. The displacement measured during the experiments was compared to the z-displacement of the indenter in the model. The peak load was evaluated for each design before 4 mm displacement, and the stiffness was compared in the linear part of the curves (between 0.02 and 0.2 mm displacement). The energy absorption was evaluated as the area under the curve up to 4 mm displacement.

For the experimental impact results, three curves were again created; a curve for the average results, a curve for one SD above, and a curve for one SD below the average curve. In the explicit FEMs, the force was evaluated in the contact pair between the rubber sheet and the indenter, and compared to the force measured experimentally. The displacement of the indenter in the model was again compared to the experimentally measured displacements. The stiffness, including the rubber sheet, was



**Table 3**

Data on cranial bone layer thickness used in the models. A part of the model is shown to visualize the different layers.



	Low thickness [mm]	Average thickness [mm]	High thickness [mm]
Inner table	0.6	1.0	1.4
Diploe	2.7	4.4	6.1
Outer table	0.8	1.3	1.8
Total thickness	4.2	6.7	9.2

compared between 1 and 2 mm displacement (the linear parts of the curves). The energy absorption was evaluated as the area under the curve up to 4 mm displacement. Additionally, the maximum indenter displacement was compared between the experiments and the simulations.

#### 2.4. Cranial bone models

FEMs were created to allow for comparison between the mechanical response of the implants and the response of cranial bone under the same impact condition. The mid-plane of the bone structures had the same shape and curvature as the implant models, with the purpose of fitting the bone structures in the same conical support as for the implant models. The thickness and material properties for the cranial bone comparison were based on data from literature. In previous FE simulations, cranial bone geometry has been created using a homogeneous (Garcia-Gonzalez et al., 2017) or a three-layered structure (Sahoo et al., 2013; Kleiven, 2007), derived based on clinical CT (De Kegel et al., 2019) or micro-CT images (Wu et al., 2018). For our study we created a three-layered structure. Large variations in thickness have been reported for the three layers, which are defined as inner and outer tables (cortical bone) and diploe (trabecular bone) (Alexander et al., 2019; Boruah et al., 2015). The inter-study variation in mean thickness likely depends on the measurement techniques (e.g. caliper, light microscopy, ultrasound, clinical CT or micro-CT), the type of cranial bone being measured (e.g. frontal, parietal or temporal bone) and subject-specific variations. Furthermore, there is no standardized method of defining the different layers. In our model, the three-layered structure was based on a recent study by Alexander et al. (2019), in which measurements were made by micro-CT. That study used 30% porosity as a threshold to separate cortical and trabecular bone. A fraction relationship was reported for the thickness of the different layers in parietal bone; 14.6% of the total thickness for the inner table, 66.0% of the total thickness for the diploe, and 19.4% of the total thickness for the outer table. We applied this relationship on the mean total thickness measured in that study ( $6.7 \pm 1.3$  mm), and defined an upper and lower bound as mean  $\pm 1.96$ SD. The thicknesses used in the cranial bone geometries can be seen in Table 3. The upper and lower bounds cover approximately 95% of a normal distribution, and a large part of the data reported on cranial thicknesses (Boruah et al., 2015).

The cranial bone was placed in the setup used for the explicit implant models. The full model included the indenter, the support, the rubber sheet, and the cranial bone. The same loading, (1.52 m/s, 5 kg) and contact definitions (indenter to rubber, rubber to bone, bone to support) as those used in the explicit implant simulations were applied. The material model used for the bone, was developed previously by Enns-Bray et al., (2018). The implementation used a non-linear material Fu-Chang Foam model with tension compression asymmetry (LS-DYNA, MAT 83). The Young's modulus values were the same as in previous studies on FE-head models (Sahoo et al., 2013): 15 GPa for cortical bone and 5 GPa for trabecular bone. These values were derived from experimental results (McElhaney et al., 1970). The

cranial bone models were solved in the explicit solver, and the force–displacement response was evaluated until peak load. The peak load and displacement at peak load were compared to the implant simulations, in addition the energy absorbed at 4 mm was calculated as the area under the curve up to 4 mm displacement. The force for the cranial bone FEMs was evaluated in the contact pair between the rubber sheet and the indenter, and the displacement at the indenter in the model.

### 3. Results

#### 3.1. Comparison between FEMs and experimental results

##### 3.1.1. Implicit models

For D1, the comparison between the implicit FEM and the experimental results is illustrated in Fig. 4. In Fig. 4a, the implicit FEM force vs. displacement response until 6 mm displacement is compared to the corresponding experimental data. Overall, the experiment and the simulation showed a similar response until the point at which the titanium failed in the experiments. From this point, the experimental force decreased while the simulated force increased. The experimental response and the simulation response had similarly shaped force-displacement curves, i.e. yield and peak force occurred at similar displacements, but the force was underestimated. The difference between the average experimental curve and the simulation in terms of the different parameters were: –35% for stiffness, –9% for peak load and –17% for energy absorbed at 4 mm displacement (Table 4). None of these parameters were within the curves created one standard deviation above and below the average curve (Table 4).

In Fig. 4b, maximum and minimum principal strains in the CaP tiles are shown for the D1 implicit FEM results. The locations in the force-displacement response, at which the strain plots were derived, are marked in Fig. 4a. Elements with a strain above failure are shown in dark red (tension) and dark blue (compression). At the CaP tile below the indenter, failure started around point one (121 N). However, failure throughout the full tile was not seen until around the second point (447 N). This point occurred close to where failure had been determined experimentally by a drop in the force response ( $463 \pm 45$  N). In Fig. 4c, the maximum and minimum principal strains are shown for the D1 implicit FEM in the titanium structure below the indenter. The highest strains were located in the deformation zones. In point four, failure strains were visible in the deformation zones – similar to what was observed experimentally.

For D2, the comparison between the implicit FEM and the experimental results can be seen in Fig. 5. The force vs. displacement response is compared in Fig. 5a. Overall, the experiment and the simulation showed a similar response. The difference between the average experimental curve and the simulation in terms of the different parameters were: –23% for stiffness, 11% for peak load and 4% for energy absorbed at 4 mm displacement (Table 4). None of these parameters were within the curves created one standard deviation above and below the average curve (Table 4).

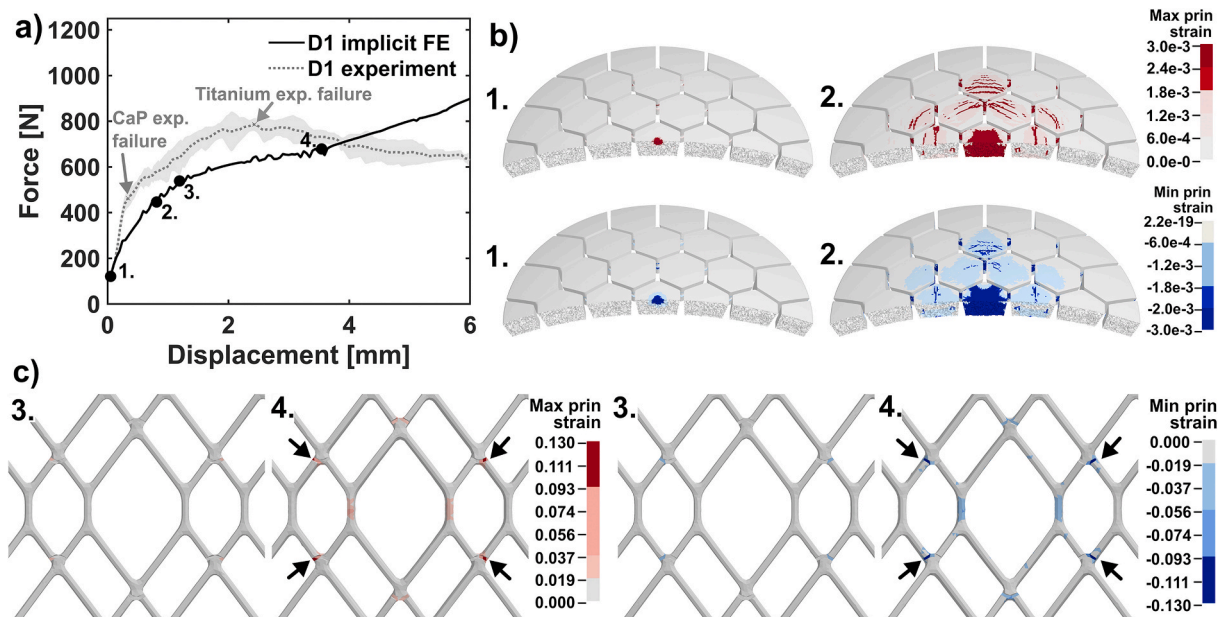


**Fig. 4.** Implicit FEM results for D1. Force vs. displacement response for the average quasi-static experimental (dotted gray line) and the implicit FEM (solid black line) (a). The gray shaded area shows one standard deviation above and below the average experimental results. In the graph, the CaP and titanium experimental failure are marked. Around these points, marked 1–4 in a), strain plots were created: point 1–121 N, point 2–447 N, point 3–538 N and point 4–679 N. Maximum (shown from the bottom) and minimum (shown from the top) strain plots for the CaP tiles (b) and for the titanium structure below the indenter (c). The failures are marked with dark red (maximum principal strain) and dark blue (minimum principal strain). The strain at yield in the titanium is marked in lighter blue and red. (For interpretation of the references to color in this figure legend, the reader is referred to the Web version of this article.)

**Table 4**  
Result from the implicit FEM and the quasi-static experiments for both designs.

	Peak load [N]	Energy at 4 mm displacement [J]	Stiffness <sup>a</sup> [N/mm]
<b>D1</b>			
Simulation	715	2.22	751
Experiment	758	2.49	936
(average - SD)			
Experiment (average)	786	2.66	1152
Experiment	843	2.84	1368
(average + SD)			
Diff. exp-average vs. simulation	−9%	−17%	−35%
<b>D2</b>			
Simulation	743	2.38	572
Experiment	653	2.22	613
(average - SD)			
Experiment (average)	669	2.28	740
Experiment	684	2.34	868
(average + SD)			
Diff. exp-average vs. simulation	11%	4%	−23%

<sup>a</sup> Between 0.02 and 0.2 mm displacement.

In Fig. 5b and c, strain plots for the D2 implicit FEM show the maximum and minimum principal strains in the CaP tiles. The locations in the force-displacement response, at which the strain plots were derived are marked in Fig. 5a. The dark red and dark blue show elements with strains above failure (Fig. 5b). At the tile below the indenter, the CaP started to show failure around the first point marked in Fig. 5a (141 N), but failure through the full tile was not seen until around the second point (449 N). This occurred close to where failure was determined experimentally ( $368 \pm 18$  N). In Fig. 5c, strain plots for the D2 implicit FEM show the maximum and minimum principal strains in the titanium structure at the third and fourth point marked in Fig. 5a. Yield strains were observed in the titanium structure below the indenter at point four,

the first peak load (743 N). No elements at this point had reached a strain above failure, failure was neither observed in the experiments at this point.

### 3.1.2. Explicit models

The comparison of results from impact experiments and explicit FEMs are presented in Fig. 6 and Table 5 for both implant designs. The overall mechanical behavior was similar for the FEMs and the experiments (Fig. 6). In the first part of the curves the simulation and experimental curves overlap for both designs. For D1, the simulated stiffness was 1% higher than derived from the average experimental force-displacement curve (Table 5). In the D1 experimental curves, the load peaked early and then decreased through the rest of the impact (Fig. 6a). This initial peak load for the FEMs was 5% lower than the average experimental peak load. In the simulation the load increased and reached a second peak load (Fig. 6a). This second peak load was 2% different from the overall peak load in the experimental average curve, and within the one standard deviation of the experimental curve peak loads (Table 5). The energy absorbed up to 4 mm displacement in the simulation was 5% higher than the average experimental results. Additionally, the maximum displacement for D1 was within a 1% difference between the experiments and simulation.

For D2, the simulated stiffness was 6% lower than the average experimental curve and fell within one standard deviation of the experimental results (Table 5). Both the experimental and simulated force vs. time curves show two peaks in the response (Fig. 6d). The first peak was captured well by the simulation, with a difference of 2% in force. For the energy absorbed at 4 mm, there was a 3% difference between experiments and the simulation (Table 5). The second peak in the average experimental curve occurred at a similar load as the first one. In the simulation the second peak load was higher than the first peak load, and 33% higher than the overall experimental peak load. For the maximum displacement, the difference between the experiments and simulation was 4%. In summary, the largest difference between the impact response from experiments and the explicit FEMs was seen in the

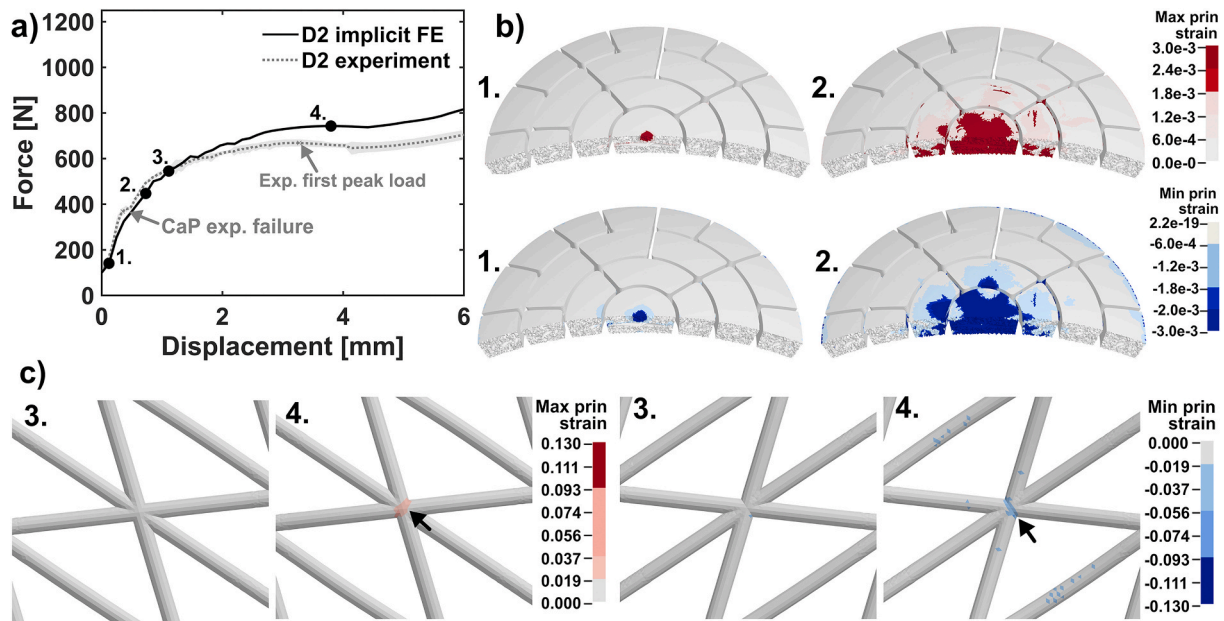


**Fig. 5.** Implicit FEM results for D2. The force vs. displacement response for the average quasi-static experimental (dotted gray line) and the implicit FEM (solid black line) (a). The gray shaded area shows one standard deviation above and below the average experimental results. In the graph, the CaP failure and the point of the first peak load from the experiments are marked. Around these points, marked 1–4 in a), strain plots were created: point 1–141 N, point 2–449 N, point 3–545 N and point 4–743 N. Maximum (shown from the bottom) and minimum (shown from the top) strain plots for the CaP tiles (b) and for the titanium structure below the indenter (c). The failures are marked with dark red (maximum principal strain) and dark blue (minimum principal strain). The strain at yield in the titanium is marked in lighter blue and red. (For interpretation of the references to color in this figure legend, the reader is referred to the Web version of this article.)

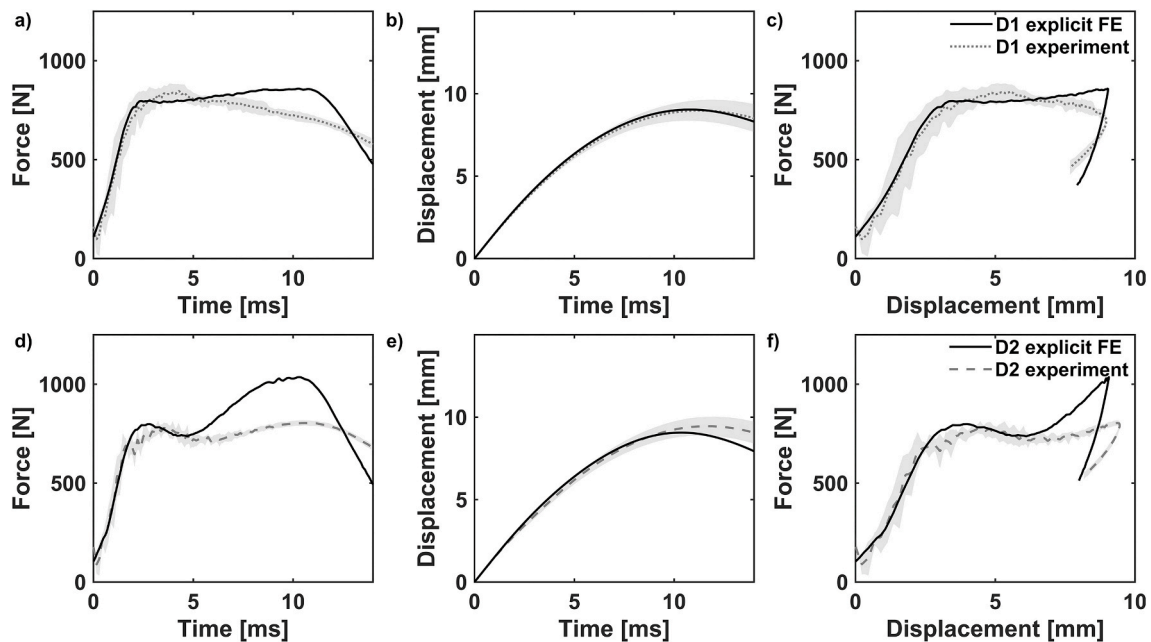


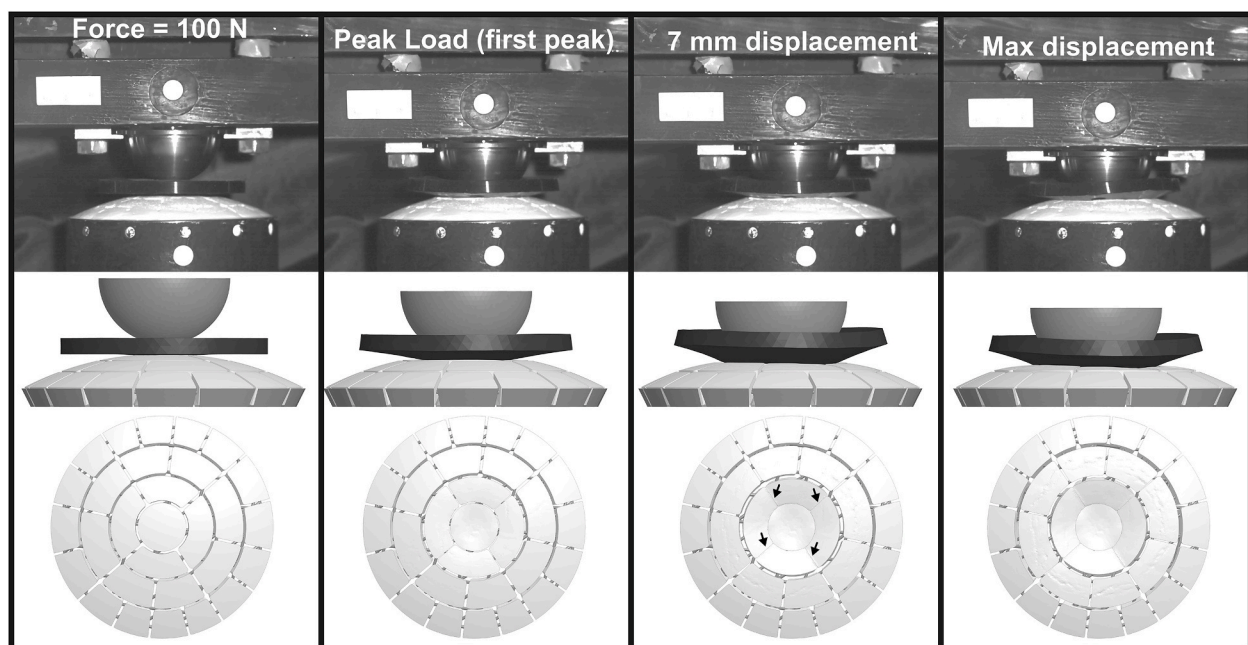
**Fig. 6.** Comparison of experimental impact test (gray dotted or dashed lines) and explicit FEM results (black solid lines). The gray shaded area shows one standard deviation above and below the average experimental results. For D1 (a–c) and D2 (d–f): Force vs. time (a and d), displacement vs. time (b and e), and force vs. displacement (c and f).



**Table 5**

Result from the explicit FEM and the impact experiments for both designs.

	Peak load first [N]	Peak load total [N]	Maximum displacement [mm]	Energy at 4 mm displacement [J]	Stiffness <sup>a</sup> [N/mm]
<b>D1</b>					
Simulation	799	859	9.1	2.1	274
Experiment (average - SD)	796	796	8.1	1.6	223
Experiment (average)	838	838	9.0	2.0	278
Experiment (average + SD)	884	884	9.7	2.4	333
Diff. exp-average vs. simulation	-5%	2%	1%	5%	1%
<b>D2</b>					
Simulation	798	1036	9.1	2.0	305
Experiment (average - SD)	753	753	8.8	1.7	293
Experiment (average)	780	780	9.5	2.0	325
Experiment (average + SD)	813	813	10.1	2.2	357
Diff. exp-average vs. simulation	-2%	33%	-4%	3%	-6%

<sup>a</sup> Between 1 and 2 mm displacement.

**Fig. 7.** Comparison of FEMs and images from the high-speed camera in the impact test for a D2 specimen: at a measured force of 100 N, at peak load (first peak), at a displacement of 7 mm and at maximum displacement. The implant is seen from the top in the lower row. In the top-view image, at 7 mm displacement, locations where the ceramic tiles come in contact are marked.

force at the second part of the impact. This difference was more pronounced in D2.

In Fig. 7, images from the high-speed camera in the impact test and the corresponding FEM, are presented for Design 2 at: a force of 100 N, peak load (first peak), a displacement of 7 mm and at maximum displacement. Overall the FEM images and the experimental images show a similar behavior. At the point where the simulations and the experimental results deviate (around 7 mm displacement), it can be observed that the CaP tiles come in contact with each other (Fig. 7).

### 3.2. Cranial bone simulation

The simulated mechanical responses for the three different bone geometries are presented in Fig. 8a–c. The thinner bone showed the lowest peak load (3607 N) and the highest displacement at peak load (4 mm) during impact. The absorbed energy at 4 mm displacement was 5.2 J. For the thin bone, the minimum and maximum principal strain at peak load are shown in Fig. 8d and e. The thin bone showed failure in both the cortical and trabecular bone after the impact. The cranial bone mainly showed compressive damage at the top (Fig. 8d), and tensile damage at the bottom (Fig. 8e). The number of elements at failure decreased with increased bone thickness. For the thick bone there was no tensile

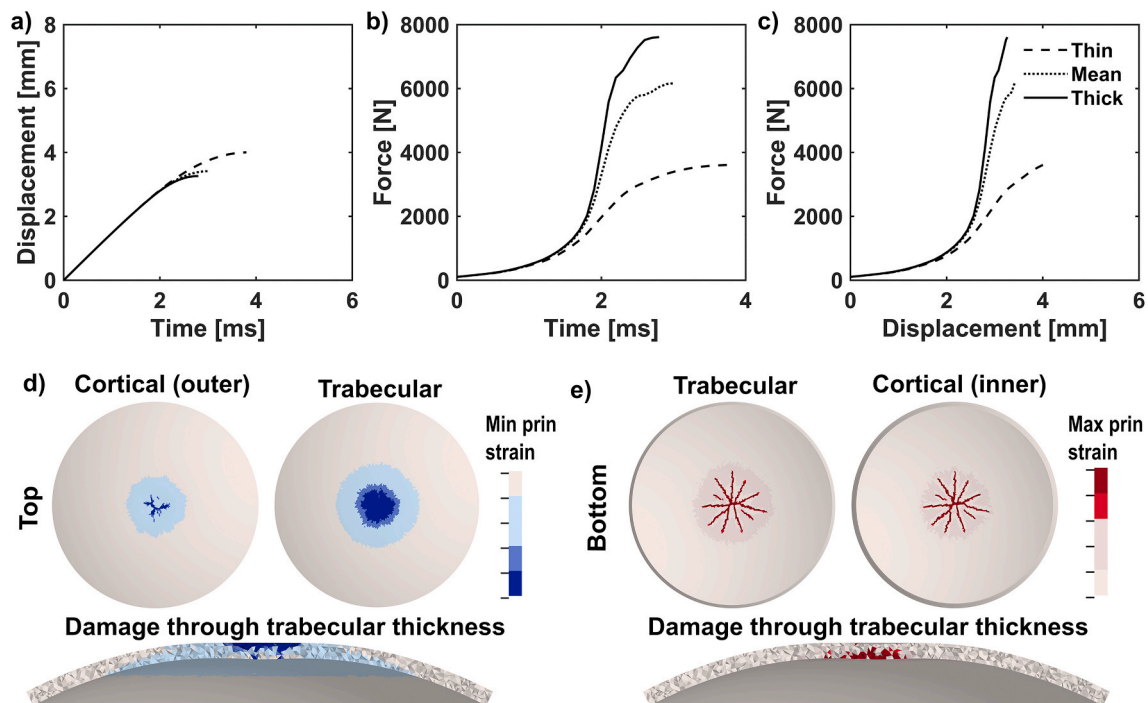


**Fig. 8.** Results from the explicit simulations of the cranial bone geometries. The displacement vs. time (a), force vs. time (b), and force vs. displacement (c) are shown for the thin, mean and thick cranial bone thickness. In the strain plots, the damage in the thin cranial bone model is shown: d) the minimum principal strains and e) the maximum principal strains. Failure in the minimum strain is shown in the darkest blue color:  $-2\%$  for the trabecular bone and  $-5.9\%$  for the cortical bone. Failure in the maximum strain is shown in the darkest red color:  $1.4\%$  for the trabecular bone and  $2.8\%$  for the cortical bone (Enns-Bray et al., 2018). (For interpretation of the references to color in this figure legend, the reader is referred to the Web version of this article.)

damage at the bottom, and the trabecular damage through the thickness was concentrated to the upper part.

#### 4. Discussion

The aim of the present study was to develop FEMs of two generic CaP-Ti cranial implant designs, and to validate the models against experimental data. The developed FEMs showed agreement with experimental data in the force-displacement response for both implant designs. The mechanical response was accurately predicted by the explicit FEMs for both designs ( $\leq 5\%$  in initial peak force) under impact loading. The implicit FEMs predicted the mechanical response of both designs but with less accuracy under quasi-static loading. The shapes of the curves were accurately predicted, but the magnitude of the force was to some extent underestimated in D1 (9%) and overestimated in D2 (11%). The second aim of the study was to predict the mechanical response of cranial bone in the same setup, and to compare it with the implant results. While damage could be seen in the thinnest cranial bone modelled, the overall energy absorption was higher in the cranial bone than in the implant.

The high accuracy of the FEMs, with respect to initial peak force and maximum displacement ( $\leq 4\%$  for both designs) under impact, will allow for mechanical optimization of CaP-Ti implants with respect to mechanical strength and cerebral protection capacity. The developed modelling approach could be used for guiding the design to target specific mechanical properties. Moreover, patient-specific implant designs could be assessed *in silico*, prior to implantation, in order to identify undesired mechanical behavior. This is of great importance since it is practically not possible to evaluate each patient-specific design experimentally. Furthermore, the impact angle, impact area etc. most likely affect the mechanical response under impact. Computational models would be an important tool in evaluating various loading scenarios. Comparison of implants from different materials and different designs is difficult since no standardized testing exists for cranial implants, FEMs

would in future studies also be useful for this assessment. Using explicit simulations, impacts could be simulated in order to assess how the different implants would fail. Validated FEMs are also useful in addressing differences in mechanical testing protocols of cranial implants. This could be of importance in order to develop standardized mechanical tests for cranial implants, which would result in more comparable test data.

To the authors' knowledge this is the first study to simulate the mechanical response of composite implants that contain a CaP material in combination with a metal. CaP materials are inherently brittle and will start to fracture as the metal deforms. In order not to overestimate the strength of the CaP material when modelling the mechanical behavior of the implant, we found it necessary to model the compression-tension asymmetry of the CaP material. Additionally, the modelling of damage was required to not overestimate the strength under impact loading. These types of models would be of interest to assess the mechanical response of other CaP composite implants, and in modelling CaP implants together with bone tissue. Previous studies which have modelled CaP material have commonly used a linear elastic material without compression-tension symmetry (Tarsuslugil et al., 2014).

A limitation in the validation of our implicit models was the rubber sheet, which was included in the experiments, but not modelled in the implicit FEMs due to convergence problems. Instead the compliance of the rubber sheet was subtracted from the experimental results. The difference in the loading scenario, could have caused the discrepancies seen between the implicit FEMs and the experimental results. Nevertheless, this does not explain why the force was underestimated in one of the models, and overestimated in the other. Likely the discretization of the very fine design features in the deformation zones could have caused the underestimation of the force in D1. The additive manufacturing of the titanium structure (L-PBF) do have limitations in accuracy of small parts, and the manufactured deformation zones might deviate from the CAD-model. The sensitivity of the discretization of the deformation

zones could be investigated in future studies to obtain a higher accuracy for the D1 implicit FEM. Moreover, since failure was not implemented for the titanium, the experimental and modelled response deviate after the titanium fractured in the D1 experiments. The overestimation of the force in D2 could be related to the insecurities in the modelling of the CaP-titanium interaction.

The explicit FEMs accurately predicted the experimental mechanical response in the first part of the impact, but in the second part the force was somewhat overestimated in the FEMs. This was more prominent for D2 than D1. Even though damage was modelled in the explicit FEMs, there was some overestimation in the impact force. As the overestimation started approximately when the CaP tiles came in contact with each other, the reason might be that the models were not fully capturing the experiments in terms of damage in the CaP tiles. In the experiments, the CaP tiles detached from the titanium structure after fracturing, and could fall through the support. This mainly occurred for the central tiles, below the indenter, these tiles also detached from the titanium structure on the unloaded side of the implant. Simulations performed in a model of only the titanium structure, without CaP tiles (supplementary material, Fig. S1) supported that the increase in force in the second peak might come from the contacts of the CaP tiles. In the simulations without CaP, D1 did not have a second peak in the force response and the second peak for D2 occurred at a lower force than the first one. To improve the modelling of CaP failure in future studies crack propagation by the extended FEM (XFEM) could e.g. be explored.

It should be noted that all material properties used in this study were defined a priori, rather than being modified to fit the computational results to the experimental data. Nevertheless, the sensitivity of the material properties in the model has not been evaluated. The CaP material has been well characterized in compression by Ajaxon et al., (2017), but with quite a high standard deviation – which is usually the case for calcium phosphate materials (Ajaxon et al., 2017). The CaP material has not yet been characterized in tension. Nevertheless, it is known that this type of materials has a much lower strength in tension. The tensile properties in our models were therefore estimated based on literature (Charrière et al., 2001). Further mechanical testing should be performed in future studies to improve the modelling of the CaP material. Additionally, the modelling of damage in composites with calcium phosphate and stronger materials could be further characterized. The titanium structure was additively manufactured with L-PBF. The material properties obtained with such a method can depend on the processing/post-processing parameters and printing direction (Zhao et al., 2016). To obtain the material properties for our models, tensile specimens were manufactured with the same cross-sectional size as the structure in the implant and using the same manufacturing method. The obtained properties were similar to previous studies testing standard sized specimen manufactured by the same method (Fousová et al., 2018; Chastand et al., 2018). Nevertheless, our small sample size ( $n = 5$ ), and the fact that only one printing direction was used could be a limitation.

Cranial bone protects the brain from impact during activities in daily life. In replacing the cranial bone with a synthetic implant, the mechanical properties of the implant in comparison to cranial bone should be of interest. This study modelled cranial bone in the same impact situation as the implants. Damage in the cranial bone was seen for all three cranial bone geometries (4 mm, 6 mm and 8 mm thickness). Damage through the full thickness was mainly seen for the bone model with 4 mm cranial bone thickness. The lowest force and largest displacement were also seen in this model. The bone model with 4 mm thickness corresponds to the lower range in reported parietal bone thickness (Alexander et al., 2019), but is also a thickness corresponding to the average temporal bone (Auperrin et al., 2014). Comparing this to the simulated impact conditions for the CaP-Ti implant, the CaP in the implant would fracture but the titanium structure would still provide protection. However, the 4 mm thick bone was still stiffer, absorbed more energy and deformed less than the CaP-Ti implant in our simulations. Even though the CaP-Ti cranial implants provide protection in

an impact and are the strongest available bioceramic based cranial implant (Lewin et al., 2020), our study would imply that full average parietal cranial bone strength is not obtained by the implant alone. However, the implant seems to provide protection in the range of the thin bone model, even though the bone absorbed more energy in the impact.

The results from this study are clinically important for estimating the strength of the implant directly after surgery. However, over time the CaP material has shown a notable ability in regenerating bone in clinical studies (Engstrand et al., 2014; Kihlström Burenstam Linder et al., 2019; Engstrand et al., 2015). These regenerative properties will potentially result in increased implant stability over time. It should be noted that our experimental setup contained considerable simplifications in terms of biofidelity, as soft tissue (scalp, dura mater, brain etc.) would provide a different damping *in vivo*. Furthermore, if the CaP tiles would fracture, they would likely be contained by soft tissue, with bone forming around the CaP tiles over time (Engstrand et al., 2014; Engstrand et al., 2015; Kihlström Burenstam Linder et al., 2019). Moreover, the cranial bone model used in this study had several simplifications. Considering the previously observed element size sensitivity in the bone material model following ultimate strain, the mechanical response of the bone was only modelled up to peak load (Enns-Bray et al., 2018). In addition, the bone geometry could have been more accurately determined by using clinical CT or micro-CT images on cranial bone specimens, and then the material properties could also have been mapped from the obtained scan densities (De Kegel et al., 2019). More studies are needed in order to evaluate the mechanical strength of the implant in comparison to cranial bone.

In summary, computational modelling allowed for a valuable comparison of the mechanical behavior of the CaP-Ti implant with cranial bone. In a similar manner, the mechanical behavior of the CaP-Ti implant could be compared to other implant materials. Furthermore, the developed modelling framework makes an important contribution to future evaluations of patient-specific CaP-Ti cranial implant designs in various loading scenarios.

## 5. Conclusions

As demonstrated by this study on two implant designs, the mechanical response of CaP-Ti composite implants can be predicted by FEMs at both quasi-static and impact loading rates. The FEMs could be a valuable tool for the design and evaluation of patient-specific CaP-Ti cranial implants to optimize their performance and assure their safety. The framework developed for modelling the CaP-Ti implant used only literature based input and matched boundary conditions, hence it could be used in future studies for modelling CaP materials in other composite implants. Compared to the CaP-Ti implant, an average parietal cranial bone model showed a stiffer response, more energy absorption and less deformation under the same impact conditions.

## Author contributions

Susanne Lewin: Conceptualization, Investigation, Visualization, Methodology, Writing - original draft, Writing - review & editing. Ingmar Fleps: Conceptualization, Investigation, Visualization, Methodology, Writing - review & editing. Dominique Neuhaus: Conceptualization, Writing - review & editing. Caroline Öhman-Mägi: Supervision, Writing - review & editing. Stephen J. Ferguson: Conceptualization, Funding acquisition, Writing - review & editing. Cecilia Persson: Conceptualization, Methodology, Supervision, Writing - review & editing, Funding acquisition. Benedikt Helgason: Conceptualization, Methodology, Supervision, Writing - review & editing.

## Declaration of competing interest

The authors declare that they have no known competing financial

interests or personal relationships that could have appeared to influence the work reported in this paper.

## Acknowledgements

Funding from the Eurostars-2 Joint European Union's Horizon 2020 (project ID: E19741) is acknowledged. The authors gratefully acknowledge Dr. Jonas Åberg at Ossdesign for discussions and assistance with the CAD-models.

## Appendix A. Supplementary data

Supplementary data to this article can be found online at <https://doi.org/10.1016/j.jmbbm.2020.104085>.

## References

- Ajaxon, I., Acciaioli, A., Lionello, G., Ginebra, M.-P., Öhman-Mägi, C., Baleani, M., Persson, C., 2017. Elastic properties and strain-to-crack-initiation of calcium phosphate bone cements: revelations of a high-resolution measurement technique. *J. Mech. Behav. Biomed. Mater.* 74, 428–437. <https://doi.org/10.1016/j.jmbbm.2017.06.023>.
- Ajaxon, I., Persson, C., 2017. Mechanical properties of brushite calcium phosphate cements. In: *The World Scientific Encyclopedia of Nanomedicine and Bioengineering II*, vol. 9. World Scientific, pp. 285–300.
- Alexander, S.L., Rafaels, K., Gunnarsson, C.A., Weerasooriya, T., 2019. Structural analysis of the frontal and parietal bones of the human skull. *J. Mech. Behav. Biomed. Mater.* 90, 689–701. <https://doi.org/10.1016/j.jmbbm.2018.10.035>.
- Ambrogio, G., Palumbo, G., Sgambitterra, E., Guglielmi, P., Piccininni, A., De Napoli, L., Villa, T., Fragoni, G., 2018. Experimental investigation of the mechanical performances of titanium cranial prostheses manufactured by super plastic forming and single-point incremental forming. *Int. J. Adv. Manuf. Technol.* 98 (5–8), 1489–1503.
- Auperrin, A., Delille, R., Lesueur, D., Bruyère, K., Masson, C., Drazetic, P., 2014. Geometrical and material parameters to assess the macroscopic mechanical behaviour of fresh cranial bone samples. *J. Biomech.* 47 (5), 1180–1185.
- Berretta, S., Evans, K., Ghita, O., 2018. Additive manufacture of PEEK cranial implants: manufacturing considerations versus accuracy and mechanical performance. *Mater. Des.* 139, 141–152.
- Bonet, J., Burton, A.J., 1998. A simple average nodal pressure tetrahedral element for incompressible and nearly incompressible dynamic explicit applications. *Commun. Numer. Methods Eng.* 14 (5), 437–449. [https://doi.org/10.1002/\(SICI\)1099-0887](https://doi.org/10.1002/(SICI)1099-0887).
- Boruah, S., Paskoff, G.R., Shender, B.S., Subit, D.L., Salzar, R.S., Crandall, J.R., 2015. Variation of bone layer thicknesses and trabecular volume fraction in the adult male human calvarium. *Bone* 77, 120–134.
- Charrière, E., Terrazzoni, S., Mordasini, P.H., Dutoit, M., Lemaître, J., Zysset, P.H., 2001. Mechanical characterization of brushite and hydroxyapatite cements. *Biomaterials* 22 (21), 2937–2945. [https://doi.org/10.1016/S0142-9612\(01\)00041-2](https://doi.org/10.1016/S0142-9612(01)00041-2).
- Chastand, V., Quaegebeur, P., Maia, W., Charkaluk, E., 2018. Comparative study of fatigue properties of Ti-6Al-4V specimens built by electron beam melting (EBM) and selective laser melting (SLM). *Mater. Char.* 143, 76–81. <https://doi.org/10.1016/j.matchar.2018.03.028>.
- De Kegel, D., Meynen, A., Famaey, N., van Lenthe, G.H., Depreitere, B., Vander Sloten, J., 2019. Skull fracture prediction through subject-specific finite element modelling is highly sensitive to model parameters. *J. Mech. Behav. Biomed. Mater.* 100, 103384.
- El Halabi, F., Rodriguez, J.F., Rebolledo, L., Hurtos, E., Doblaré, M., 2011. Mechanical characterization and numerical simulation of polyether-ether-ketone (PEEK) cranial implants. *J. Mech. Behav. Biomed. Mater.* 4 (8), 1819–1832.
- Engstrand, T., 2012. Biomaterials and biologics in craniofacial reconstruction. *J. Craniofac. Surg.* 23 (1), 239–242.
- Engstrand, T., Kihlström, L., Lundgren, K., Trobos, M., Engqvist, H., Thomsen, P., 2015. Bioceramic implant induces bone healing of cranial defects. *Plast. Reconstr. Surg. Glob. Open* 3 (8). <https://doi.org/10.1097/GOX.0000000000000467>.
- Engstrand, T., Kihlström, L., Neovius, E., Docherty Skogh, A.-C., Lundgren, T.K., Jacobsson, H., Bohlén, J., Åberg, J., Engqvist, H., 2014. Development of a bioactive implant for repair and potential healing of cranial defects. *J. Neurosurg.* 120 (1), 273–277.
- Enns-Bray, W.S., Bahaloo, H., Fleps, I., Ariza, O., Gilchrist, S., Widmer, R., Guy, P., Pålsson, H., Ferguson, S.J., Crompton, P.A., Helgason, B., 2018. Material mapping strategy to improve the predicted response of the proximal femur to a sideways fall impact. *J. Mech. Behav. Biomed. Mater.* 78, 196–205. <https://doi.org/10.1016/j.jmbbm.2017.10.033>.
- Fousová, M., Vojtěch, D., Doubrava, K., Daniel, M., Lin, C.-F., 2018. Influence of inherent surface and internal defects on mechanical properties of additively manufactured Ti6Al4V alloy: comparison between selective laser melting and electron beam melting. *Materials* 11 (4), 537. <https://doi.org/10.3390/ma11040537>.
- García-González, D., Jayamohan, J., Sotiropoulos, S.N., Yoon, S.H., Cook, J., Siviour, C.R., Arias, A., Jérusalem, A., 2017. On the mechanical behaviour of PEEK and HA cranial implants under impact loading. *J. Mech. Behav. Biomed. Mater.* 69, 342–354. <https://doi.org/10.1016/j.jmbbm.2017.01.012>.
- Kihlström Burenstam Linder, L., Birgersson, U., Lundgren, K., Illies, C., Engstrand, T., 2019. Patient-specific titanium-reinforced calcium phosphate implant for the repair and healing of complex cranial defects. *World Neurosurg.* 122, e399–e407. <https://doi.org/10.1016/j.wneu.2018.10.061>.
- Kleiven, S., 2007. Predictors for Traumatic Brain Injuries Evaluated through Accident Reconstructions. SAE Technical Paper.
- Lethaus, B., Bloebaum, M., Koper, D., Poort-ter Laak, M., Kessler, P., 2014. Interval cranioplasty with patient-specific implants and autogenous bone grafts – success and cost analysis. *J. Cranio-Maxillo-Fac. Surg.* 42 (8), 1948–1951. <https://doi.org/10.1016/j.jcms.2014.08.006>.
- Lethaus, B., Safi, Y., ter Laak-Poort, M., Kloss-Brandstätter, A., Banki, F., Robbenmenke, C., Steinseifer, U., Kessler, P., 2011. Cranioplasty with customized titanium and PEEK implants in a mechanical stress model. *J. Neurotrauma* 29 (6), 1077–1083. <https://doi.org/10.1089/neu.2011.1794>.
- Lewin, S., Åberg, J., Neuhaus, D., Engqvist, H., Ferguson, S.J., Öhman-Mägi, C., Helgason, B., Persson, C., 2020. Mechanical behaviour of composite calcium phosphate-titanium cranial implants: effects of loading rate and design. *J. Mech. Behav. Biomed. Mater.* 104, 103701. <https://doi.org/10.1016/j.jmbbm.2020.103701>.
- Marcián, P., Narra, N., Borák, L., Chamrad, J., Wolff, J., 2019. Biomechanical performance of cranial implants with different thicknesses and material properties: a finite element study. *Comput. Biol. Med.* 109, 43–52.
- Matic, D.B., Manson, P.N., 2004. Biomechanical analysis of hydroxyapatite cement cranioplasty. *J. Craniofac. Surg.* 15 (3), 415–422.
- McElhaney, J.H., Fogle, J.L., Melvin, J.W., Haynes, R.R., Roberts, V.L., Alem, N.M., 1970. Mechanical properties of cranial bone. *J. Biomech.* 3 (5), 495–511.
- Ono, I., Tateshita, T., Nakajima, T., Ogawa, T., 1998. Determinations of strength of synthetic hydroxyapatite ceramic implants. *Plast. Reconstr. Surg.* 102 (3), 807–813.
- Persson, J., Helgason, B., Engqvist, H., Ferguson, S.J., Persson, C., 2018. Stiffness and strength of cranioplastic implant systems in comparison to cranial bone. *J. Cranio-Maxillo-fac. Surg. Off. Publ. Eur. Assoc. Cranio-Maxillo-fac. Surg.* 46 (3), 418–423. <https://doi.org/10.1016/j.jcms.2017.11.025>.
- Piitulainen, J.M., Mattila, R., Moritz, N., Vallittu, P.K., 2017. Load-bearing capacity and fracture behavior of glass fiber-reinforced composite cranioplasty implants. *J. Appl. Biomater. Funct. Mater.* 15 (4), e356–e361. <https://doi.org/10.5301/jabfm.5000375>.
- Pittet, C., Lemaître, J., 2000. Mechanical characterization of brushite cements: a Mohr circles' approach. *J. Biomed. Mater. Res.* 53 (6), 769–780. [https://doi.org/10.1002/1097-4636\(2000\)53:6<769::aid-jbm19>3.0.co](https://doi.org/10.1002/1097-4636(2000)53:6<769::aid-jbm19>3.0.co).
- Ridwan-Pramana, A., Marcián, P., Borák, L., Narra, N., Forouzanfar, T., Wolff, J., 2016. 'Structural and mechanical implications of PMMA implant shape and interface geometry in cranioplasty-A finite element study'. *J. Cranio-Maxillo-Fac. Surg.* 44 (1), 34–44.
- Ridwan-Pramana, A., Marcián, P., Borák, L., Narra, N., Forouzanfar, T., Wolff, J., 2017. Finite element analysis of 6 large PMMA skull reconstructions: a multi-criteria evaluation approach. *PLoS One* 12 (6), e0179325. <https://doi.org/10.1371/journal.pone.0179325>.
- Sahoo, D., Deck, C., Yoganandan, N., Willinger, R., 2013. Anisotropic composite human skull model and skull fracture validation against temporo-parietal skull fracture. *J. Mech. Behav. Biomed. Mater.* 28, 340–353.
- Sundblom, J., Nowinski, D., Casar-Borota, O., Rytteflors, M., 2018. Removal of giant intrasosseous meningioma followed by cranioplasty using a custom-made bioceramic implant: case report. *J. Neurosurg.* 1–5. <https://doi.org/10.3171/2018.4.JNS1850>.
- Tarsuslugil, S.M., O'Hara, R.M., Dunne, N.J., Buchanan, F., Orr, J.F., Barton, D.C., Wilcox, R.K., 2014. Experimental and computational approach investigating burst fracture augmentation using PMMA and calcium phosphate cements. *Ann. Biomed. Eng.* 42 (4), 751–762.
- van de Vijfeijken, S.E.C.M., Munker, T.J.A.G., Spijker, R., Karssemakers, L.H.E., Vandertorp, W.P., Becking, A.G., Ubbink, D.T., 2018. Autologous bone is inferior to alloplastic cranioplasties: safety of autograft and allograft materials for cranioplasties, a systematic review. *World Neurosurg.* 117, 443–452. <https://doi.org/10.1016/j.wneu.2018.05.193>.
- Wu, Q., Ma, L., Feng, L., Wang, Z., Ohrndorf, A., Christ, H.-J., Xiong, J., 2018. Impact response and energy absorption of human skull cellular bones. *J. Mech. Behav. Biomed. Mater.* 81, 106–119. <https://doi.org/10.1016/j.jmbbm.2018.02.018>.
- Zegers, T., ter Laak-Poort, M., Koper, D., Lethaus, B., Kessler, P., 2017. The therapeutic effect of patient-specific implants in cranioplasty. *J. Cranio-Maxillo-Fac. Surg.* 45 (1), 82–86. <https://doi.org/10.1016/j.jcms.2016.10.016>.
- Zhao, X., Li, S., Zhang, M., Liu, Y., Sercombe, T., Wang, S., Hao, Y., Yang, R., Murr, L.E., 2016. Comparison of the microstructures and mechanical properties of Ti-6Al-4V fabricated by selective laser melting and electron beam melting. *Mater. Des.* 95, 21–31. <https://doi.org/10.1016/j.matdes.2015.12.135>.
- ISO 7743:2017, Rubber, vulcanized or thermoplastic — Determination of compression stress-strain properties, the International Organization for Standardization (ISO). [https://www.iso.org/cms/render/live/en/sites/isoorg/co\\_ntents/data/standard/07/27/72784.html](https://www.iso.org/cms/render/live/en/sites/isoorg/co_ntents/data/standard/07/27/72784.html) (accessed Feb. 15, 2020).